



# Impact of porous silicon thickness on thermoelectric properties of silicon-germanium alloy films produced by electrochemical deposition of germanium into porous silicon matrices followed by rapid thermal annealing

Nikita Grevtsov<sup>a,\*</sup>, Eugene Chubenko<sup>a</sup>, Ilya Gavrilin<sup>b</sup>, Dmitry Goroshko<sup>c</sup>, Olga Goroshko<sup>c</sup>, Ilya Tsiniainkin<sup>d</sup>, Vitaly Bondarenko<sup>a</sup>, Maksim Murtazin<sup>b</sup>, Alexey Dronov<sup>b</sup>, Sergey Gavrilov<sup>b</sup>

<sup>a</sup> Belarusian State University of Informatics and Radioelectronics, Minsk, Belarus

<sup>b</sup> National Research University of Electronic Technology, Zelenograd, Moscow, Russia

<sup>c</sup> Institute of Automation and Control Processes, Far Eastern Branch, Russian Academy of Sciences, Vladivostok, Russia

<sup>d</sup> Lomonosov Moscow State University, Moscow, Russia

## ARTICLE INFO

### Keywords:

Porous silicon  
Electrochemical deposition  
Silicon-germanium  
Thermoelectric materials  
Thin films

## ABSTRACT

Silicon-germanium alloy films were formed by electrochemical deposition of germanium into porous silicon matrices with thicknesses varying from 1.5 to 10  $\mu\text{m}$  followed by subsequent rapid thermal processing at 950  $^{\circ}\text{C}$  in an inert atmosphere. Study of the fabricated structures using SEM and Raman spectroscopy, as well as measurements of their electrical conductivity and thermoelectric properties revealed that the highest Seebeck coefficient ( $-505 \mu\text{V}/\text{K}$  at 450 K) and Power Factor ( $1950 \mu\text{W}/(\text{m}\cdot\text{K}^2)$  at 400 K) values were obtained when a 5  $\mu\text{m}$ -thick porous silicon was used as a structural matrix. Under such conditions, an optimal balance between electrical conductivity, structural disorder and electrical insulation from the substrate is achieved due to the presence of a residual porous underlayer, making it possible to maximize the film's thermoelectric performance. The obtained silicon-germanium alloy films are deemed suitable for the fabrication of both discrete and integrated thermoelectric devices based on monocrystalline silicon substrates.

## 1. Introduction

Thermoelectric systems are an important element of the energy harvesting concept aimed at obtaining electricity from non-fossil fuels [1,2]. Thermoelectric materials are able to convert “otherwise-wasted” heat from industrial sources, as well as “clean” thermal energy from renewable sources into electric power using the Seebeck effect [3]. Thermoelectric devices based thereon are praised for their simplicity, scalability, reliability, absence of any toxic, sonic or vibration emissions and ability to operate at a high power density [1–7]. However, thermoelectric devices are characterized by relatively low efficiency compared to other alternative renewable power sources. In the best experimental results thermoelectric efficiency  $\eta$  does not exceed 12–13 % [8]. The efficiency value of a given thermoelectric device is usually described by the dimensionless figure-of-merit coefficient  $ZT$ . This parameter is proportional to temperature  $T$ , Seebeck coefficient  $S$  and

electrical conductivity  $\sigma$ , and inversely proportional to thermal conductivity  $\kappa$  in accordance with the equation [2,9]:

$$ZT = \frac{\sigma TS^2}{\kappa} \quad (1)$$

Therefore, in order to raise the efficiency of a thermoelectric device based on a given material, it is necessary to either increase its electrical conductivity and Seebeck coefficient or decrease its thermal conductivity.

Thermal conductivity comprises of electronic and lattice components. The electronic component is directly tied to electrical conductivity, while the lattice component is related to phonon interactions [10]. Both components can be affected by point defects, nanostructuring, doping and other factors, leading to increased crystal structure disorder [8,9,11–13]. Thus, to achieve an optimal balance of parameters and maximize thermoelectric efficiency, meticulous

\* Corresponding author.

E-mail address: [hrautsou@gmail.com](mailto:hrautsou@gmail.com) (N. Grevtsov).

<https://doi.org/10.1016/j.mssp.2024.109148>

Received 24 September 2024; Received in revised form 6 November 2024; Accepted 19 November 2024

Available online 21 November 2024

1369-8001/© 2024 Elsevier Ltd. All rights are reserved, including those for text and data mining, AI training, and similar technologies.

selection of materials and processing methods thereof must be conducted.

Silicon-germanium alloys (SiGe, Si<sub>1-x</sub>Ge<sub>x</sub>) are known to be prominent candidates for high-temperature thermoelectric applications [14]. The abundance of both silicon and germanium, as well as the alloy's good electrical conductivity and reduced thermal conductivity compared to pure crystalline silicon gives SiGe an economical and technical edge over most of its functional counterparts [7,15–17]. Despite having already been used for heat-to-electricity conversion for many years as part of long-duration space missions [15], silicon-germanium is currently being considered yet again for a variety of terrestrial applications [17].

Thermoelectric properties and applicability of SiGe alloys can be additionally improved by preparing them in the form of thin films. Compared to traditional bulk alloys formed using legacy semiconductor processing techniques [18] or a variety of powder metallurgy approaches [19], thin films offer some unique advantages such as greatly increased scalability and improved electrophysical characteristics due to nanostructuring. Currently-employed approaches to fabricating thin films of SiGe include liquid-phase epitaxy [20], chemical vapor deposition [21], laser sintering after suspension coating [22], as well as layer exchange [23]. Unfortunately, these methods require complex equipment or expensive gaseous precursors, and a search for a simpler approach remains an important task.

Recently our research group has developed a new approach to producing SiGe thin films by electrodepositing germanium into mesoporous silicon (mesoPS) matrices followed by a rapid thermal processing (RTP) step [24–26]. The proposed method is simple and suitable for low-cost mass production of devices based on SiGe alloy thin films. It was successfully employed to produce both *n*-type (phosphorus- or antimony-doped) and *p*-type (boron-doped) materials, with the doping type and level determined by those of the initial silicon wafer. Modulation of structural parameters of nanostructured mesoPS layers used as initial substrates was expected to additionally reduce the alloy's thermal conductivity, providing improved thermoelectric characteristics. It is known that room temperature thermal conductivity of PS exhibits a 50 % or more drop from the 156 W (m K)<sup>-1</sup> value inherent to bulk monocrystalline silicon [27], and partial oxidation leads to a significant (up to two orders of magnitude) further reduction [28].

The above arguments led us to the idea of employing a mesoPS buffer layer to insulate the SiGe film, reducing the shunting effect of the substrate and enhancing the overall thermoelectric performance. To achieve this, thicker PS layers should be employed for the alloy's formation. The influence of a mesoPS matrix thickness on thermoelectric properties of *n*-type SiGe thin films fabricated on monocrystalline silicon substrates using the proposed approach is the subject of the present work.

## 2. Materials and methods

MesoPS matrices were anodically formed at a current density of 70 mA/cm<sup>2</sup> on highly antimony-doped (0.01 Ohm-cm) monocrystalline *n*<sup>+</sup>-type silicon wafers with a (100) surface orientation. An electrolyte containing hydrofluoric acid (HF), deionized water and isopropyl alcohol mixed in a volume ratio of 1:3:1 was employed for the anodization process. MesoPS layers with four different thickness values were prepared: 1.5, 3, 5, and 10 μm, formed at anodization times of 30, 60, 100, and 240 s, respectively. Prior to germanium deposition, a thin (about 0.3 μm) subsurface mesoPS layer possessing smaller pore sizes and a lower porosity was removed from each sample using a two-step method [29,30]. On the first step displacement deposition of copper from a CuSO<sub>4</sub>/HF solution was conducted. Afterwards, as a second step, the deposited metal and the displaced silicon layer were both etched in nitric acid [30]. Lastly, the mesoPS samples were immersed in concentrated HF (45 %) to dissolve any excess SiO<sub>2</sub> formed during nitric acid exposure.

Germanium electrodeposition was carried out in the same processing

regime for all the prepared mesoPS matrices. For this purpose, an aqueous solution containing 0.05 M GeO<sub>2</sub>, 0.01 M InCl<sub>3</sub>, 0.5 M K<sub>2</sub>SO<sub>4</sub> and 0.1 M succinic acid was employed, and electrolysis was conducted at a current density of 2 mA/cm<sup>2</sup> with constant stirring at 85 °C for 30 min. Due to the presence and simultaneous deposition of indium, growth of germanium primarily occurred on the samples' surfaces and proceeded in accordance with the electrochemical liquid-liquid-solid (ec-LLS) mechanism, with the resulting deposits consisting of intertwining germanium nanowires [24].

Both electrochemical processes were performed using a Metrohm Autolab PGSTAT302N potentiostat/galvanostat and a PTFE electrochemical cell with a horizontally-oriented silicon wafer working electrode located at the bottom of the cell pressed down into a graphite backside contact plate and a platinum wire counter-electrode placed above the wafer parallel to its surface.

Silicon-germanium alloy films were obtained by RTP of the as-prepared samples at 950 °C for 30 s under argon flow (800 sccm) using an Annealsys As-One 100 RTP system. It should be noted that significant restructuring of PS is observed significantly below the melting point of bulk silicon (1414 °C) [31]. According to our preliminary results, RTP conducted at 950 °C on PS without any germanium deposits causes partial melting of its sidewalls to already be observed in a subsurface layer roughly 2–3 μm thick. This sintered layer also possesses slightly larger pore diameters, allowing molten germanium to more easily gain access into them. The areas below remain largely unaffected, which can likely be attributed to them being subjected to smaller temperature values due to gradient heat transfer into the bulk wafer. Considering the above, the employed temperature value is high enough to both melt down the surface-adjacent germanium deposits and sinter them together with the mesoPS side-walls, forming an alloyed film in the subsurface area of each sample. For thicker PS layers, areas deeper than this subsurface region remain unalloyed due to insufficient temperatures and obstructions towards the flow of liquid germanium, and SiGe films partially insulated by the underlying PS layers of varying thicknesses are obtained, all exhibiting distinct electrophysical parameters.

The described sample fabrication route is schematically illustrated by Fig. 1. The illustrations in question are based on the cross-section scanning electron microscope (SEM) imagery presented in subsequent sections.

The samples' morphology was studied using a Zeiss Supra-40 SEM. An Inlens SE detector was employed with an aperture of 30 μm and an accelerating voltage set to 10 kV. Raman spectra were obtained using an NTEGRA Spectra II confocal Raman spectrometer. Excitation was carried out by a He-Ne laser with constant pumping at a wavelength of ~633 nm, as well as two semiconductor lasers emitting at wavelengths of 473 and 785 nm, operated at 1.45, 1.00 and 8.60 mW of optical power, respectively. The radiation was focused on the sample using an 100× objective with a numerical aperture of 0.9 into a spot with a diameter of about 1.5 μm.

The study of electrical conductivity and Seebeck coefficient of SiGe alloy film samples was carried out in the temperature range of 80–450 K using a specialized Cryotel setup. To ensure stable contact of the measuring probes to the samples and substrates, gold-antimony (AuSb) contact pads were deposited onto the surface of SiGe and annealed at 450 °C in an argon atmosphere for 20 min to improve electrical contact. Electrical conductivity and Seebeck coefficient values were measured as effective parameters with contribution from the both the formed alloy film and the underlying monocrystalline silicon substrate due to high conductivity of the latter.

## 3. Results

The initially obtained mesoPS matrices possess a uniform structure, with pores oriented perpendicularly to the surface of the monocrystalline silicon wafer (Fig. 2). No significant difference in the

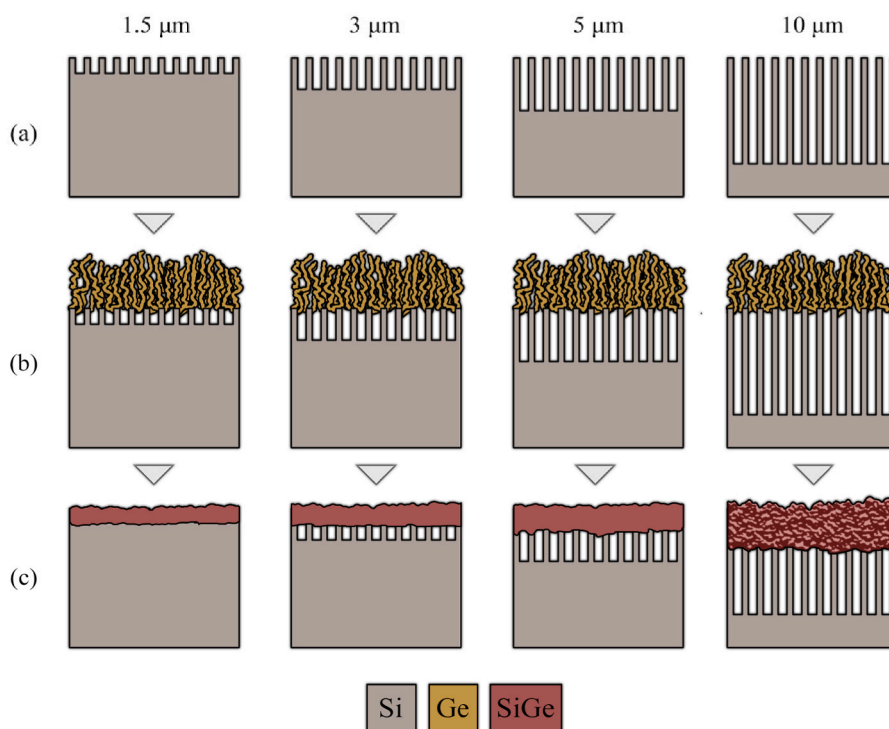


Fig. 1. – Schematic illustration of the samples' fabrication route: (a) initial mesoPS matrices with varying thicknesses; (b) germanium nanowires electrochemically deposited onto mesoPS; (c) formation of an alloy film after RTP.

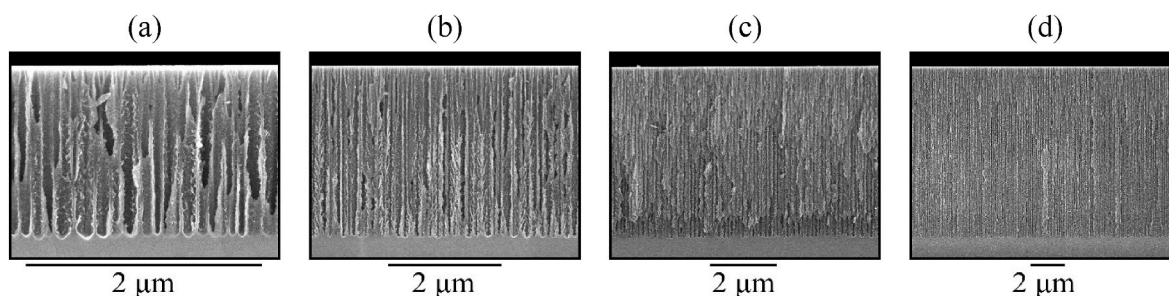


Fig. 2. – Cross-section SEM images of initial mesoPS matrices with varying thicknesses used for SiGe alloy formation.

morphology of porous layers obtained at different anodization times is observed, apart from their thickness. The pores possess diameters ranging from 110 to 130 nm and are surrounded by side-walls varying from 24 to 36 nm in width. These values remain nearly unchanged along each layer's depth.

As a result of germanium electrodeposition, a thick layer of intertwined germanium nanowires is formed on top of each mesoPS layer (Fig. 3). The layer's average thickness measures at about 10 μm, but is

fairly uneven due to its growth mechanism.

As a result of RTP, the germanium layer melts down and undergoes alloying with the pore sidewalls. SEM images of the resulting alloy layers (Fig. 4) clearly demonstrate the dependence of their morphology on the initial matrix thickness. At the minimum thickness of 1.5 μm the sintered film is densely packed above the substrate's surface and appears fairly uniform, exhibiting a well-defined film/substrate interface. At higher thicknesses, however, alloying is reproducibly accompanied by the

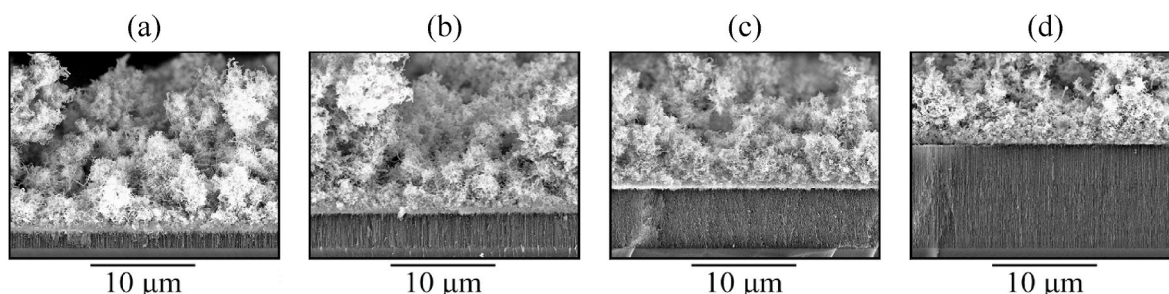


Fig. 3. – Cross-section SEM images of mesoPS matrices with varying thicknesses subsequently to germanium electrodeposition.

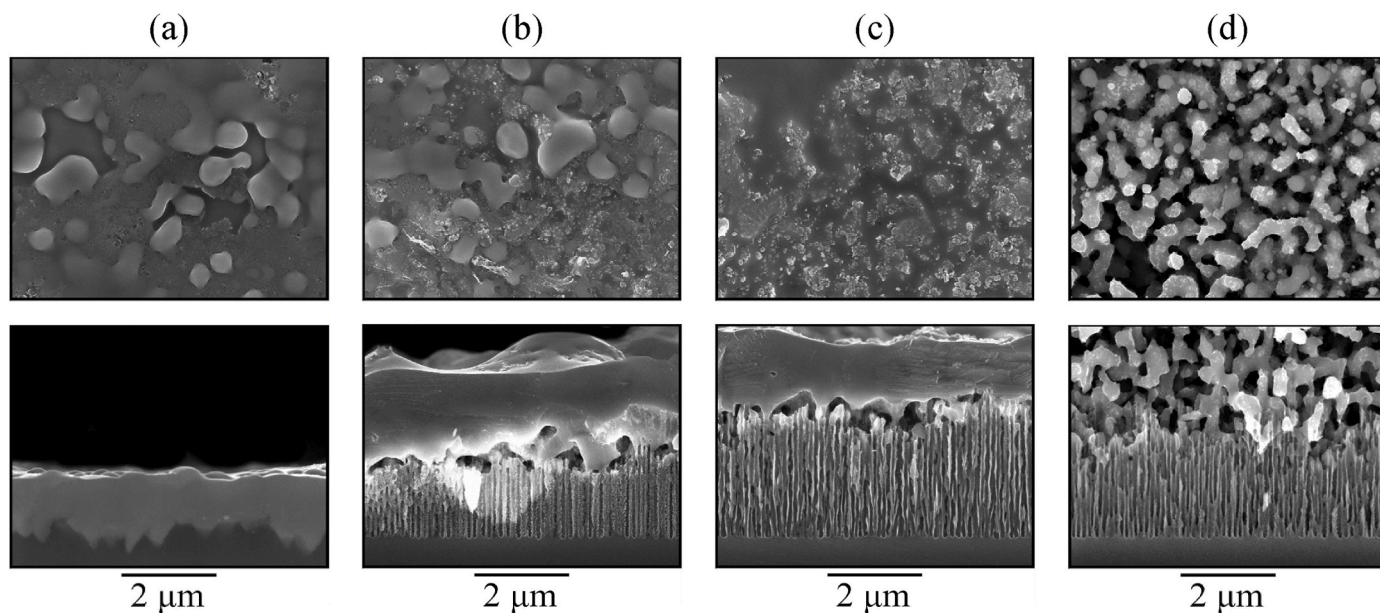


Fig. 4. – (Top row) surface and (bottom row) cross-section SEM images of alloy films based on mesoPS matrices with four different thicknesses: (a) 1.5 μm, (b) 3 μm, (c) 5 μm, (d) 10 μm.

presence of a residual PS layer located directly under the film, with its thickness proportional to that of the matrix. The alloy film thickness varies from 1.0 to 1.5 μm for 3–5 μm-thick PS matrices to 4 μm for a 10 μm-thick matrix. In the latter case, the alloy film itself also becomes porous, exhibiting pronounced and well-developed inner microstructuring.

Raman spectra of the obtained samples recorded at different excitation wavelengths reveal characteristic vibrational modes of SiGe alloys present therein (Fig. 5). The presented Raman spectra were normalized and fitted by a number of asymmetric double sigmoid functions. Penetration depth of laser radiation into a given material is determined by its energy, i.e. wavelength. Each material’s absorption, on the other hand, differs from the other’s. The alloy with germanium contents of around  $x = 0.40$  is known to exhibit absorption depths of around 80 nm, 4 μm and >5 μm for 473, 633 and 785 nm laser radiation, correspondingly [32]. In other words, a 473 nm laser enables data

acquisition from a very thin subsurface layer, a 633 nm laser — from the entire alloy film, and the 785 nm laser — from regions all the way down to the alloy/substrate interface.

The obtained Raman spectra exhibit three prominent bands located at 290, 405 and 480  $\text{cm}^{-1}$ , which correspond to vibrational modes of germanium-germanium (Ge-Ge, marked as red), silicon-germanium (Si-Ge, blue) and silicon-silicon (Si-Si, green) bonds in the SiGe alloy [33–36]. The peaks in question are asymmetrical, which may indicate presence of low-dimensional effects, surface states, defects and the material becoming non-stoichiometric [37,38]. The exact positions of Raman scattering peaks for each sample registered at different excitation wavelengths are listed in Table 1.

It is well-established that positions of Raman bands and their peak intensities correlate with the composition of a given SiGe alloy [33–36]. Notably, for samples with initial mesoPS matrix thicknesses ranging from 1.5 to 5 μm, an increase in laser radiation penetration depth causes

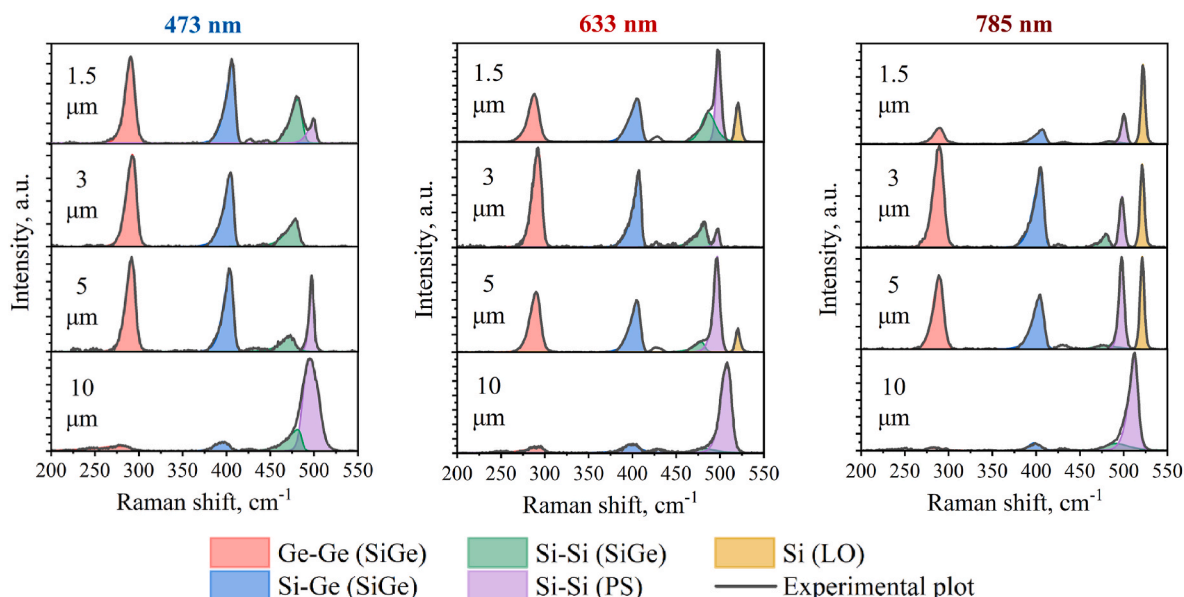


Fig. 5. – Raman spectra of alloy films based on mesoPS matrices with varying thicknesses, recorded at different wavelengths.

**Table 1**

– Positions of bands present on Raman spectra recorded at different laser wavelengths.

Initial mesoPS matrix thickness, $\mu\text{m}$	Laser wavelength, nm	Raman band position, $\text{cm}^{-1}$				
		Ge-Ge (SiGe)	Si-Ge (SiGe)	Si-Si (SiGe)	Si-Si (PS)	Si (LO)
1.5	473	290.6	405.5	479.5	498.9	–
	633	288.7	404.9	485.4	497.7	521.0
	785	289.3	406.8	480.3	499.7	521.0
3	473	292.2	404.5	478.6	–	–
	633	292.7	408.2	482.7	497.7	–
	785	289.3	403.4	479.5	498.4	521.0
5	473	291.6	402.6	472.8	496.9	–
	633	290.2	404.8	481.5	499.2	521.0
	785	288.2	404.6	475.7	497.8	521.0
10	473	280.3	396.5	480.5	496.3	–
	633	295.1	402.1	480.1	508.2	–
	785	282.6	396.7	485.9	511.9	–

Ge-Ge peak positions to shift towards lower frequencies, and Si-Ge and Si-Si — to higher frequencies. For the sample with the initial mesoPS layer thickness of 10  $\mu\text{m}$ , the Si-Si peak is only revealed after fitting. It overlaps with another pronounced band located at 497–500  $\text{cm}^{-1}$ , which corresponds to silicon-silicon bonds in mesoPS side-wall crystallites (marked as Si-Si (PS), purple in Fig. 5).

Si-Si (PS) is a triple degenerative optical vibrational mode of monocrystalline silicon Si(LO) in the center of the Brillouin zone shifted to lower frequencies as a result of melting, amorphization and distortion of crystal structure during PS formation, germanium deposition and alloying [39,40]. It is relatively weak on spectra recorded for 1.5 and 3  $\mu\text{m}$  samples, but its intensity gradually increases with laser penetration depth and matrix thickness. For the 10  $\mu\text{m}$  sample under 633 and 785 nm laser radiation, this band is found at even higher frequencies of 507–512  $\text{cm}^{-1}$ , becoming closer to another prominent peak observed at 521  $\text{cm}^{-1}$  (marked as Si(LO), yellow in Fig. 5). The latter is also only observed at 633 and 785 nm and likely occurs due to the accumulation of signal from the underlying monocrystalline silicon substrate [41]. Si (LO) is not observed for the thickest porous layer, indicating that laser radiation does not propagate to the substrate and is fully absorbed and/or scattered by the alloy and thick residual PS.

We employed the following known equations to determine the composition of obtained  $\text{Si}_{1-x}\text{Ge}_x$  alloy films at different depths [34,35, 42,43]:

$$\frac{I_{\text{Si-Si}}}{I_{\text{Si-Ge}}} = \frac{A(1-x)}{2x}, \quad (2)$$

$$\frac{I_{\text{Ge-Ge}}}{I_{\text{Si-Ge}}} = \frac{Bx}{2(1-x)}, \quad (3)$$

where  $I$  is the intensity of corresponding peaks on Raman spectra, and  $A$  and  $B$  are empirical coefficients that serve to compensate the resonance effects leading to the dependence of band intensity on excitation wavelength. In this case,  $A = 1.5$  and  $B = 1.8$  were used, which account for the widest possible range of germanium concentrations in SiGe [44].

The calculated germanium atomic concentration values are presented in Table 2. In most cases germanium concentration is slightly higher in the bottommost part of the alloy film, with the last sample serving as the only exception. Assumingly, for a very thick mesoPS layer, laser radiation penetrates into the residual PS region where little to no germanium is present, leading to a decrease in the recorded concentration value.

Electrical resistivity of the obtained alloy films increases with the initial mesoPS matrix thickness throughout the whole studied temperature range (Fig. 6,a). Resistivity of the 10  $\mu\text{m}$  sample is approximately 50 % higher than that of the monocrystalline silicon substrate and reaches 0.012 Ohm-cm at 300 K, with the substrate measuring at 0.008

**Table 2**

– Calculated germanium fractions in alloy films based on mesoPS matrices with varying thicknesses calculated based on Raman spectra recorded at different excitation laser wavelengths.

Initial mesoPS matrix thickness, $\mu\text{m}$	Laser wavelength, nm	Calculated germanium fractions $x$ in $\text{Si}_{1-x}\text{Ge}_x$
1.5	473	0.519
	633	0.510
	785	0.527
3	473	0.563
	633	0.591
	785	0.579
5	473	0.517
	633	0.522
	785	0.562
10	473	0.215
	633	0.486
	785	0.304

Ohm-cm at the same temperature. It should be noted that during resistivity measurements the alloy film was shunted by the highly conductive silicon substrate underneath it. As such, the obtained resistivity value is an effective parameter and does not directly correspond to the absolute value of film's resistivity, but does depend on it.

Seebeck coefficient values remain negative for all the samples (Fig. 6, b), indicating n-type conductivity. The coefficient's absolute value increases with the thickness of the initial mesoPS matrix: the highest values are exhibited by samples based on 5 and 10  $\mu\text{m}$  PS, with curves corresponding to these samples nearly overlapping with each other. Notably, in a higher temperature range of 300–470 K the Seebeck coefficient of the 5  $\mu\text{m}$  sample was further increased and reached  $-505 \mu\text{V/K}$  at 450 K, which is a relatively high value compared to results presented in other works [15–17]. The initial substrate demonstrates a value of only  $-271 \mu\text{V/K}$  at the same temperature.

The Power Factor of the obtained alloy films increases with temperature (Fig. 6, c). The highest values of 1940–1960  $\mu\text{W}/(\text{m}\cdot\text{K}^2)$  were obtained for the 5  $\mu\text{m}$  sample in the temperature range of 350–410 K. Both 5 and 10  $\mu\text{m}$  samples exhibit a pronounced Power Factor maximum in this range followed by a steady decrease.

Temperature increase in the film can be determined by the modes of oscillations localized within it using an approach known as Raman thermometry. Stokes and anti-Stokes Raman spectra represent processes involving emission and absorption of phonons, and the intensity ratio of corresponding non-resonant peaks is proportional to phonon population. The sample's temperature can then be calculated using Boltzmann statistics, and the alloy film temperature can be determined from localized vibrational modes [45]. The temperature difference between the alloy film and bulk silicon underneath it  $\Delta T$  is determined by the value of the alloy thermal conductivity  $\kappa$ , the input power  $P$ , the thickness of the absorbing region of the film  $L$  in the direction normal to the surface  $c$  the cross-sectional area  $A$ . Then, according to Fourier's law of heat conduction,  $\kappa$  is equal to [46].

$$\kappa = \frac{P L}{\Delta T A}. \quad (4)$$

The thermal conductivity value at 300 K achieved for the alloy based on a 1.5  $\mu\text{m}$  sample is 3.6  $\text{Wm}^{-1}\text{K}^{-1}$  — 2–4 times less than that of bulk SiGe alloys of similar composition [10], and is comparable to some experimental values obtained for thin-film samples [9]. It amounts to a room temperature  $ZT$  value of 0.1. However, we were unable to ascertain  $\kappa$  and  $ZT$  for other samples based on 3, 5 and 10  $\mu\text{m}$  PS layers using this method, as the increasingly thick porous layer made the laser radiation unable to reach the underlying monocrystalline silicon wafer, even in the case when a 785 nm laser was employed.

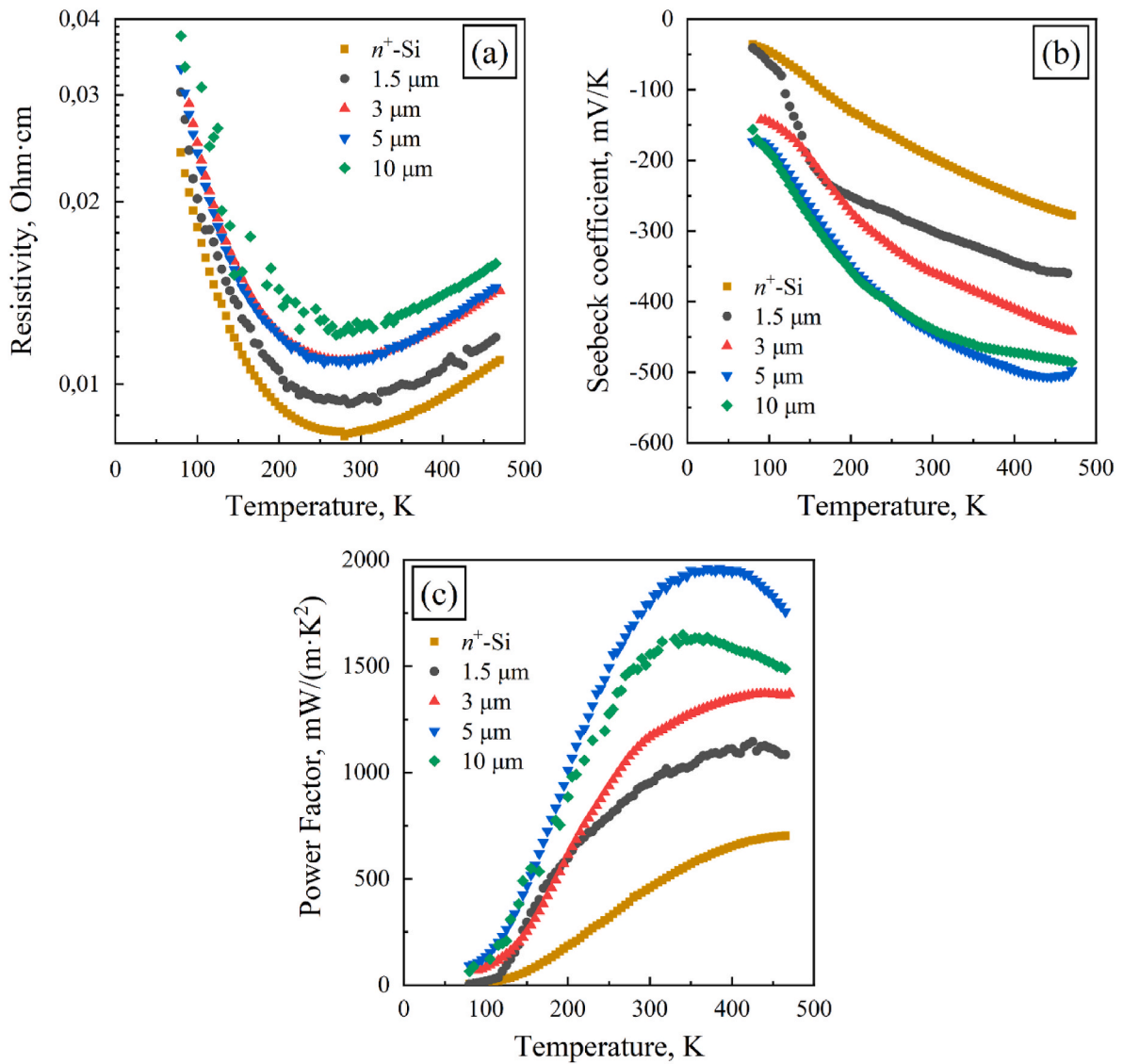


Fig. 6. – Temperature dependence of (a) resistivity, (b) Seebeck coefficient and (c) Power Factor of the obtained alloy films compared to those of the initial monocrystalline silicon substrate.

#### 4. Discussion

According to the results of thermoelectric parameter measurements, an increase in mesoPS matrix thickness leads to an increase in both the Seebeck coefficient and the Power Factor of the resulting alloys. We surmise that the residual underlying PS layer visible on SEM images of thicker samples (Fig. 4, b, c, d) plays a crucial role in this phenomenon, as it could electrically and thermally insulate the alloy film formed on top of it from the substrate. As was mentioned in the introduction section, room temperature thermal conductivity of PS is over two times smaller than that of monocrystalline silicon [28]. Similarly, electrical conductivity of mesoPS layers with porosities above 50 % is strongly affected by a multitude of complex factors (surface states, quantum confinement in silicon crystallites, oxidation, etc.) and is also generally lower than in the bulk material [28]. Considering the above, it's likely that a mesoPS layer can minimize the influence of the underlying monocrystalline silicon substrate, which otherwise acts as a shunt and interferes with electrical and thermoelectric measurements.

The proposed resistance model illustrating differences in conductivity depending on residual PS thickness is schematically illustrated in Fig. 7. Here the resistors  $R_{SiGe||}$  and  $R_{Si}$  correspond to the lateral

resistances of the SiGe film and the monocrystalline silicon substrate, respectively.  $R_{SiGe\perp}$  represents the resistance of the SiGe film in the direction perpendicular to the substrate's surface. It includes the resistance of the alloy film itself, as well as that of the Si/SiGe heterojunction. Here we assume that the alloyed SiGe film can be considered electrically isotropic and that  $R_{SiGe\perp}$  is lower than  $R_{SiGe||}$ , as the distance between electrical contacts on the surface is much higher than the film's thickness.

In complete absence of residual PS (Fig. 7, a) the SiGe film is in direct electrical contact with the highly doped substrate. Based on the results of resistivity measurements (Fig. 6, a), we assume that the SiGe film possesses a higher resistivity value than the silicon substrate, and a part of the electrical current flows through a shunting circuit consisting of  $2R_{SiGe\perp}$  and  $R_{Si}$ .

The use of moderately thick porous matrices (3–5  $\mu\text{m}$ ) results in the presence of an underlying low-conductivity ( $R_{PS} \gg R_{Si}$ ) residual porous layer after RTP (Fig. 7, b and Fig. 4, b, c) [28]. The SiGe film is separated from the underlying substrate, but is still uniform, and its resistivity is expected to remain stable. Hence, the overall shunting circuit resistance increases by  $2R_{PS}$ . Under these favorable conditions, the prepared alloy films are less affected by the substrate's conductivity and provide higher

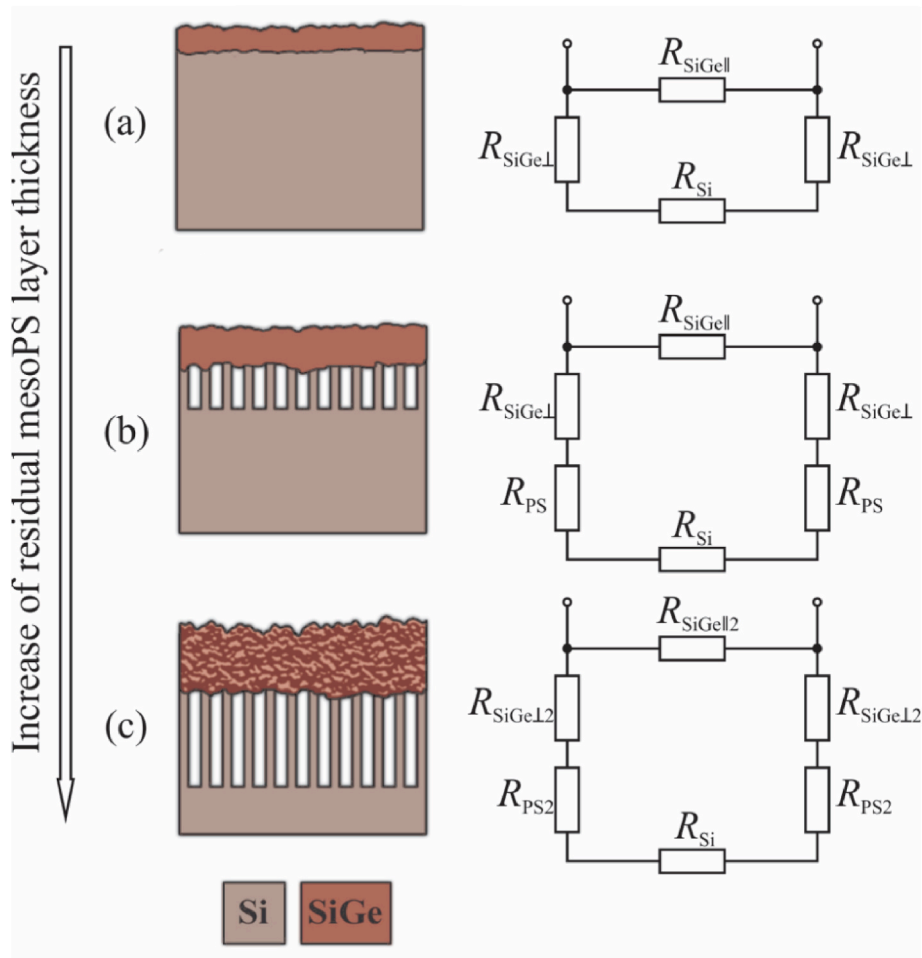


Fig. 7. – Equivalent circuits of SiGe film/Si substrate systems with varying thicknesses of residual porous layers observed subsequently to RTP, as determined by the thickness of an initial porous matrix: (a) 1.5 μm, (b) 3–5 μm and (c) 10 μm.

Seebeck coefficient and Power Factor values (Fig. 6b and c).

Based on the registered thermoelectric characteristics, 5 μm can be deemed an optimal initial mesoPS thickness for subsequent SiGe alloy formation. For the 10 μm sample, the overly thick layer negatively affects germanium deposition and alloy formation, with the latter becoming fragmented and porous (Fig. 4). Germanium distribution across the sample’s cross section also undergoes noticeable changes compared to samples with thinner PS layers (Table 2), with peak germanium concentration shifting towards the central part of the structure. Additionally, the Si-Si vibrational mode on the Raman spectra becomes weaker and overlaps with the peak corresponding to Si-Si bonds in mesoPS crystallites. All these changes indicate a higher degree of structural disorder and insufficient alloying due to uneven germanium distribution. Structural disorder increases the resistivity of the alloy film up to a certain value reflected by the resistance  $R_{SiGeL2} > R_{SiGeL}$  (see Fig. 7, c). These negative factors greatly outweigh the benefits of improved electrical insulation from the substrate provided by a thicker layer with a higher resistivity  $R_{PS2} > R_{PS}$ .

On the other hand, based solely on Raman spectroscopy data, an optimal structure for the SiGe film formation appears to correspond to the matrix thickness of 3 μm. Raman spectra of the sample in question obtained at 473 nm exhibit no signs of any PS skeleton remnants. In contrast, for the 5 μm sample, despite its better thermoelectric characteristics, a “Si-Si mesoPS” peak emerges under the same conditions, while under higher wavelength lasers the peak corresponding to the Si-Si bonds in the alloy overlaps with the “Si-Si mesoPS”, similarly to the 10 μm sample. These factors indicate a higher degree of structural

disorder in the bottommost part of the 5 μm sample. A decrease in Power Factor at temperatures above 400 K also negatively affects the performance of alloy samples based on 5 and 10 μm matrices. As such, an optimal PS matrix thickness may somewhat vary depending on the specific application case.

### 5. Conclusion

It has been shown that, by adjusting the thickness of the initial mesoPS matrix layer, it is possible to enhance thermoelectric properties of SiGe alloys formed by electrochemical deposition of germanium into PS with subsequent RTP conducted at 950 °C for 30 s in an inert atmosphere. Raising the mesoPS layer thickness from 1.5 to 5 μm allowed for an increase in Seebeck coefficient from –358 up to –505 μV/K at 450 K. It also resulted in an almost twofold increase in Power Factor from 1100 to 1950 μW/(m·K<sup>2</sup>) at 400 K.

It is deduced that the observed enhancement of thermoelectric properties with an increase in PS thickness is a consequence of the corresponding increase in the degree of electrical insulation of the alloy film from the underlying highly doped silicon substrate. However, an exceedingly high PS layer thicknesses may also negatively affect the structural integrity of a SiGe alloy film formed on it, resulting in degradation of its thermoelectric properties. As such, a balance between these two factors must be maintained to ensure optimal thermoelectric performance, encouraging the use PS layers with carefully adjusted thicknesses.

The obtained results open up new opportunities to construct highly

effective thermoelectric devices on silicon substrates, which could also be integrated with circuitry or power modules formed on the same substrate.

### CRedit authorship contribution statement

**Nikita Grevtsov:** Writing – review & editing, Methodology, Investigation, Formal analysis. **Eugene Chubenko:** Writing – original draft, Methodology. **Ilya Gavrilin:** Investigation, Funding acquisition. **Dmitry Goroshko:** Software, Investigation. **Olga Goroshko:** Investigation. **Iliia Tsiniiaikin:** Investigation. **Vitaly Bondarenko:** Writing – review & editing, Resources, Project administration, Investigation. **Maksim Murtazin:** Investigation. **Alexey Dronov:** Investigation. **Sergey Gavrilov:** Project administration, Funding acquisition.

### Funding

This research was financially supported by the Russian Science Foundation (project № 20-19-00720, <https://rscf.ru/project/20-19-00720/>).

### Declaration of competing interest

The authors declare that they have no known competing financial interests or personal relationships that could have appeared to influence the work reported in this paper.

### Acknowledgments

We would like to thank D. Zhigulin (State Center “Belmicroanalysis”, Affiliate Research & Design Center “Belmicrosystems”, JSC “INTEGRAL”, Minsk, Belarus) for performing SEM analysis of the experimental samples. Tsiniiaikin I.I. thanks the BASIS Foundation for the Advancement of Theoretical Physics and Mathematics.

### Data availability

Data will be made available on request.

### References

- [1] M. Feng, S. Lv, J. Deng, Y. Guo, Y. Wu, G. Shi, M. Zhang, An overview of environmental energy harvesting by thermoelectric generators, *Renew. Sustain. Energy Rev.* 187 (2023) 113723, <https://doi.org/10.1016/j.rser.2023.113723>.
- [2] M. d'Angelo, C. Galassi, N. Lecis, Thermoelectric materials and applications: a review, *Energies* 16 (2023) 6409, <https://doi.org/10.3390/en16176409>.
- [3] A. Polozine, S. Sirovinskaya, L. Schaeffer, History of development of thermoelectric materials for electric power generation and criteria of their quality, *Mater. Res.* 17 (2014) 1260–1267, <https://doi.org/10.1590/1516-1439.272214>.
- [4] G.S. Nolas, J. Poon, M. Kanatzidis, Recent developments in bulk thermoelectric materials, *MRS Bull.* 31 (2006) 199–205, <https://doi.org/10.1557/mrs2006.45>.
- [5] Z. Soleimani, S. Zoras, B. Ceranic, S. Shahzad, Y. Cui, A review on recent developments of thermoelectric materials for room-temperature applications, *Sustain. Energy Technol. Assessments* 37 (2020) 100604, <https://doi.org/10.1016/j.seta.2019.100604>.
- [6] W. Sun, R. Sui, G. Yuan, H. Zheng, Z. Zeng, P. Xie, L. Yuan, Z. Ren, F. Cai, Q. Zhang, Thermoelectric module design to improve lifetime and output power density, *Mater. Today Phys.* 18 (2021) 100391, <https://doi.org/10.1016/j.mtphys.2021.100391>.
- [7] X. Zhang, L.-D. Zhao, Thermoelectric materials: energy conversion between heat and electricity, *J. Materio.* 1 (2015) 92–105, <https://doi.org/10.1016/j.jmat.2015.01.001>.
- [8] B. Ryu, J. Chung, M. Kumagai, T. Mato, Y. Ando, S. Gunji, A. Tanaka, D. Yana, M. Fujimoto, Y. Imai, Y. Katsura, S. Park, Best thermoelectric efficiency of ever-explored materials, *iScience* 26 (2023) 106494, <https://doi.org/10.1016/j.isci.2023.106494>.
- [9] D.M. Rowe (Ed.), *CRC Handbook of Thermoelectrics*, CRC Press, Boca Raton, FL, 1995.
- [10] Q. Xu, J. Zhou, T.-H. Liu, G. Chen, Effect of electron-phonon interaction on lattice thermal conductivity of SiGe alloys, *Appl. Phys. Lett.* 115 (2019) 023903, <https://doi.org/10.1063/1.5108836>.

- [11] C.J. Vineis, A. Shakouri, A. Majumdar, M.G. Kanatzidis, Nanostructured thermoelectrics: big efficiency gains from small features, *Adv. Mater.* 22 (2010) 3970–3980, <https://doi.org/10.1002/adma.201000839>.
- [12] D.M. Rowe, V.S. Shukla, The effect of phonon-grain boundary scattering on the lattice thermal conductivity and thermoelectric conversion efficiency of heavily doped fine-grained, hot-pressed silicon germanium alloy, *J. Appl. Phys.* 52 (1981) 7421–7426, <https://doi.org/10.1063/1.328733>.
- [13] A.J. Minnich, M.S. Dresselhaus, Z.F. Ren, G. Chen, Bulk nanostructured thermoelectric materials: current research and future prospects, *Energy Environ. Sci.* 2 (2009) 466, <https://doi.org/10.1039/b822664b>.
- [14] S. Maeda, T. Ishiyama, T. Nishida, T. Ozawa, N. Saitoh, N. Yoshizawa, T. Suemasu, K. Toko, High thermoelectric performance in polycrystalline GeSiSn ternary alloy thin films, *ACS Appl. Mater. Interfaces* 14 (2022) 54848–54854, <https://doi.org/10.1021/acsami.2c14785>.
- [15] B. Cook, Silicon-germanium: the legacy lives on, *Energies* 15 (2022) 2957, <https://doi.org/10.3390/en15082957>.
- [16] P. Chiang, S. Hu, W.-T. Yen, H.-J. Wu, H.-P. Hsu, C. Lan, A study of iron-doped SiGe growth for thermoelectric applications, *J. Alloys Compd.* 967 (2023) 171700, <https://doi.org/10.1016/j.jallcom.2023.171700>.
- [17] N.M. Ravindra, B. Jariwala, A. Bañobre, A. Maske, Thermoelectrics: material candidates and structures I – chalcogenides and silicon-germanium alloys, in: *Thermoelectrics*, Springer International Publishing, Cham, 2019, pp. 69–89, [https://doi.org/10.1007/978-3-319-96341-9\\_5](https://doi.org/10.1007/978-3-319-96341-9_5).
- [18] N.V. Abrosimov, V.N. Kurlov, R. Schewski, J. Winkler, Automated growth of Si<sub>1-x</sub>Ge<sub>x</sub> single crystals with constant axial gradient by czochralski technique, *Cryst. Res. Technol.* 55 (2020) 1900097, <https://doi.org/10.1002/crat.201900097>.
- [19] R. Basu, A. Singh, High temperature Si-Ge alloy towards thermoelectric applications: a comprehensive review, *Mater. Today Phys.* 21 (2021) 100468, <https://doi.org/10.1016/j.mtphys.2021.100468>.
- [20] D. Yoon, H. Shin, S. Oh, C. Jo, K. Lee, S. Jung, D.-H. Ko, Characteristics of high-order silane based Si and SiGe epitaxial growth under 600 °C, *J. Cryst. Growth* 632 (2024) 127642, <https://doi.org/10.1016/j.jcrysgro.2024.127642>.
- [21] C. Schwinge, K. Kühnel, J. Emara, L. Roy, K. Biedermann, W. Weinreich, S. Kolodinski, M. Wiatr, G. Gerlach, M. Wagner-Reetz, Optimization of LPCVD phosphorous-doped SiGe thin films for CMOS-compatible thermoelectric applications, *Appl. Phys. Lett.* 120 (2022) 031903, <https://doi.org/10.1063/5.0076945>.
- [22] K. Xie, M.C. Gupta, Thermoelectric properties of SiGe thin films prepared by laser sintering of nanograin powders, *J. Alloys Compd.* 820 (2020) 153182, <https://doi.org/10.1016/j.jallcom.2019.153182>.
- [23] K. Toko, S. Maeda, T. Ishiyama, K. Nozawa, M. Murata, T. Suemasu, Layer exchange synthesis of SiGe for flexible thermoelectric generators: a comprehensive review, *Adv. Elect. Mater.* 10 (2024) 2400130, <https://doi.org/10.1002/aelm.202400130>.
- [24] E.B. Chubenko, N.L. Grevtsov, V.P. Bondarenko, I.M. Gavrilin, A.V. Pavlikov, A. A. Dronov, L.S. Volkova, S.A. Gavrilov, Raman spectra of silicon/germanium alloy thin films based on porous silicon, *J. Appl. Spectrosc.* 89 (2022) 829–834, <https://doi.org/10.1007/s10812-022-01432-3>.
- [25] N. Grevtsov, E. Chubenko, V. Bondarenko, I. Gavrilin, A. Dronov, S. Gavrilov, Germanium electrodeposition into porous silicon for silicon-germanium alloying, *Materialia* 26 (2022) 101558, <https://doi.org/10.1016/j.mta.2022.101558>.
- [26] N. Grevtsov, E. Chubenko, V. Bondarenko, I. Gavrilin, A. Dronov, S. Gavrilov, G. Rymyski, K. Yanushkevich, D. Goroshko, E. Argunov, Composition-adjustable silicon-germanium alloy films based on porous silicon matrices, *Mater. Today Commun.* 38 (2024) 107886, <https://doi.org/10.1016/j.mtcomm.2023.107886>.
- [27] C.J. Glassbrenner, G.A. Slack, Thermal conductivity of silicon and germanium from 3°K to the melting point, *Phys. Rev.* 134 (1964) A1058–A1069, <https://doi.org/10.1103/PhysRev.134.A1058>.
- [28] L. Canham (Ed.), *Handbook of Porous Silicon*, second ed., Springer, Cham, 2018, <https://doi.org/10.1007/978-3-319-71381-6>, 2018.
- [29] E.B. Chubenko, S.V. Redko, A.I. Sherstnyov, V.A. Petrovich, D.A. Kotov, V. P. Bondarenko, Influence of the surface layer on the electrochemical deposition of metals and semiconductors into mesoporous silicon, *Semiconductors* 50 (2016) 372–376, <https://doi.org/10.1134/S1063782616030040>.
- [30] H. Bandarenka, S.L. Prischepa, R. Fittipaldi, A. Vecchione, P. Nenzi, M. Balucani, V. Bondarenko, Comparative study of initial stages of copper immersion deposition on bulk and porous silicon, *Nanoscale Res. Lett.* 8 (2013) 85, <https://doi.org/10.1186/1556-276X-8-85>.
- [31] M.K. Sahoo, P. Kale, Restructured porous silicon for solar photovoltaic: a review, *Microporous Mesoporous Mater.* 289 (2019) 109619, <https://doi.org/10.1016/j.micromeso.2019.109619>.
- [32] J. Humlíček, M. Garriga, M.I. Alonso, M. Cardona, Optical spectra of Si<sub>x</sub>Ge<sub>1-x</sub> alloys, *J. Appl. Phys.* 65 (1989) 2827–2832, <https://doi.org/10.1063/1.342720>.
- [33] A.A. Shklyayev, V.A. Volodin, M. Stoffel, H. Rinnert, M. Vergnat, Raman and photoluminescence spectroscopy of SiGe layer evolution on Si(100) induced by dewetting, *J. Appl. Phys.* 123 (2018) 015304, <https://doi.org/10.1063/1.5009720>.
- [34] M.I. Alonso, K. Winer, Raman spectra of c - Si<sub>1-x</sub>Ge<sub>x</sub> alloys, *Phys. Rev. B* 39 (1989) 10056–10062, <https://doi.org/10.1103/PhysRevB.39.10056>.
- [35] P.M. Mooney, F.H. Dacol, J.C. Tsang, J.O. Chu, Raman scattering analysis of relaxed Ge<sub>x</sub>Si<sub>1-x</sub> alloy layers, *Appl. Phys. Lett.* 62 (1993) 2069–2071, <https://doi.org/10.1063/1.109481>.
- [36] F. Pezzoli, E. Bonera, E. Grilli, M. Guzzi, S. Sanguinetti, D. Christina, G. Isella, H. Von Känel, E. Wintersberger, J. Stangl, G. Bauer, Raman spectroscopy determination of composition and strain in heterostructures, *Mater. Sci. Semicond. Process.* 11 (2008) 279–284, <https://doi.org/10.1016/j.mssp.2008.09.012>.

- [37] Y. Gao, P. Yin, Origin of asymmetric broadening of Raman peak profiles in Si nanocrystals, *Sci. Rep.* 7 (2017) 43602, <https://doi.org/10.1038/srep43602>.
- [38] V.I. Korepanov, D.M. Sedlovets, An asymmetric fitting function for condensed-phase Raman spectroscopy, *Analyst* 143 (2018) 2674–2679, <https://doi.org/10.1039/C8AN00710A>.
- [39] M. Kadlečíková, J. Breza, L. Vančo, M. Mikolášek, M. Hubeník, J. Racko, J. Greguš, Raman spectroscopy of porous silicon substrates, *Optik* 174 (2018) 347–353, <https://doi.org/10.1016/j.ijleo.2018.08.084>.
- [40] S.R. Goodes, T.E. Jenkins, M.I.J. Beale, J.D. Benjamin, C. Pickering, The characterisation of porous silicon by Raman spectroscopy, *Semicond. Sci. Technol.* 3 (1988) 483–487, <https://doi.org/10.1088/0268-1242/3/5/011>.
- [41] J.H. Parker, D.W. Feldman, M. Ashkin, Raman scattering by silicon and germanium, *Phys. Rev.* 155 (1967) 712–714, <https://doi.org/10.1103/PhysRev.155.712>.
- [42] S.A. Mala, L. Tsybeskov, D.J. Lockwood, X. Wu, J.-M. Baribeau, Raman scattering in Si/SiGe nanostructures: revealing chemical composition, strain, intermixing, and heat dissipation, *J. Appl. Phys.* 116 (2014) 014305, <https://doi.org/10.1063/1.4886598>.
- [43] J.C. Tsang, P.M. Mooney, F. Dacol, J.O. Chu, Measurements of alloy composition and strain in thin Ge x Si1-x layers, *J. Appl. Phys.* 75 (1994) 8098–8108, <https://doi.org/10.1063/1.356554>.
- [44] V.A. Volodin, M.D. Efremov, A.S. Deryabin, L.V. Sokolov, Determination of the composition and stresses in GexSi(1-x) heterostructures from Raman spectroscopy data: refinement of model parameters, *Semiconductors* 40 (2006) 1314–1320, <https://doi.org/10.1134/S106378260611011X>.
- [45] S. Sandell, E. Chávez-Ángel, A. El Sachat, J. He, C.M. Sotomayor Torres, J. Maire, Thermoreflectance techniques and Raman thermometry for thermal property characterization of nanostructures, *J. Appl. Phys.* 128 (2020) 131101, <https://doi.org/10.1063/5.0020239>.
- [46] N. Grevtsov, E. Chubenko, V. Bondarenko, I. Gavrilin, A. Dronov, S. Gavrilov, D. L. Goroshko, O. Goroshko, G.S. Rimski, K. Yanushkevich, Thermoelectric materials based on cobalt-containing sintered silicon-germanium alloys. <https://doi.org/10.2139/ssrn.4936024>, 2024.